Study of the reactions $\pi^- p \to \pi^+ \pi^- n$ and $\pi^- p \to K^+ K^- n$ at 1.98 and 2.41 GeV/c †

R. J. Leeper and M. Buttram
Sandia Laboratories, Albuquerque, New Mexico 87115
and Ames Laboratory-ERDA and Department of Physics, Iowa State University, Ames, Iowa 50011

H. B. Crawley, D. W. Duke,* R. C. Lamb, and F. C. Peterson
Ames Laboratory-ERDA and Department of Physics, Iowa State University, Ames, Iowa 50011
(Received 14 March 1977)

We have studied the reactions $\pi^- p \to \pi^+ \pi^- n$ and $\pi^- p \to K^+ K^- n$ at 1.98 and 2.41 GeV/c over a dimeson mass range from 0.75 to 1.23 GeV/c^2. Final-state neutrons were detected near 0° corresponding to $|t - t_{\min}| < 0.003$ (GeV/c)^2 near a dimeson mass of 1.0 GeV/c^2. Charged particles were detected in the Argonne Effective Mass Spectrometer and/or scintillation detectors surrounding the hydrogen target. The mass of the dimeson was calculated from the beam and neutron four-vectors, the latter being determined by the measured flight time of the neutrons, with a mass resolution of $\sigma = 4$ MeV/c^2. One of the prominent features of the $\pi^+ \pi^-$ mass spectrum is a sharp break near 0.95 GeV/c^2. This feature and the rapid rise of the $K^+ K^-$ spectrum near threshold are analyzed in terms of the parameters of the S^* resonance. In the kinematic region covered by our data the contribution of the ρ meson is small. The 62000 $\pi^+ \pi^-$ events (11000 three-constraint and 51000 one-constraint) and the 470 $K^+ K^-$ events (all four-constraint) were analyzed with both a Breit-Wigner and a K-matrix formulation with various parameterizations of the background. Consistent values of the S^* pole parameters were obtained in all of the various types of analyses for both beam momenta. An average of the parameters from these fits gives the position of the S^* pole to be $(969 \pm 5) - i\,(15 \pm 4)$ MeV/c^2, compared to the present world average of $(993.2 \pm 4.4) - i(20.0 \pm 3.7)$ MeV/c^2.

I. INTRODUCTION

For effective masses near 1 GeV/c^2 the production cross sections for s-wave isospin-zero dimeson systems ($\pi\pi$ or KK) are dominated by the S^* resonance. Both the rapid drop in the cross section for the process $\pi^- p \to \pi^+ \pi^- n$ near dipion mass 950 MeV/c^2 and the rapid rise above threshold for the reaction $\pi^- p \to K^+ K^- n$ have been explained in terms of a pole in the s-wave $\pi\pi$ scattering amplitude near $K^+ K^-$ threshold, the S^*. The position of the S^* pole was originally calculated from scattering-length fits to the $K^0 \bar{K}^0$ spectrum.[1] However, the pole value has never been well determined by KK data alone. The pole position may be determined rather more accurately from $\pi^+ \pi^-$ mass spectra[2] but only after the s-wave contribution to the data has been separated from the somewhat larger high-mass tail of the ρ. The separated spin-zero contribution is then fitted to a slowly varying background plus an interfering Breit-Wigner term or, more commonly, to a K-matrix formalism. (The K-matrix parameters may be Taylor expansions in mass giving the M matrix.) The fit results are then used to compute the S^* pole value.

The separation of the s-wave and p-wave contributions normally is made using a phase-shift analysis. This background subtraction has the potential for introducing systematic errors in the computed pole position. It is therefore important to cross check this type of analysis with results from experiments involving different backgrounds. One way in which the large ρ contribution to the p-wave background may be removed is by studying the $\pi^0 \pi^0$ spectrum through the (900 to 1000)-MeV/c^2 mass range.[3] To date, the advantage of this method has been largely offset by the experimental difficulties inherent in such measurements. Typically the ratio of s wave to background is worse in these data than in $\pi^+ \pi^-$ data.

We have discovered that the ρ contribution to the $\pi^+ \pi^-$ mass spectrum is strongly suppressed in a particular kinematic regime. Specifically we observe that very little ρ is produced near a beam momentum of 2 GeV/c for extreme forward production.[4] This tendency for ρ production to drop in the forward direction has been observed before.[2] With minimal p-wave contamination in the $\pi^+ \pi^-$ mass spectrum the data may be analyzed without recourse to a phase-shift analysis.

In this paper we present the data from an experiment which studied $\pi^+ \pi^-$ (and $K^+ K^-$) production in this ρ suppressed regime. In order to carry out our investigation we studied meson production in the reaction $\pi^- p \to X^0 n$, where X^0 is a meson system. Data reported in this paper were taken at two different incident π^- momenta, namely 1.98 and 2.41 GeV/c. The 1.98-GeV/c data spanned the missing-mass region from approximately 750 to 1080 MeV/c^2. The 2.41-GeV/c data spanned the missing-mass region from approximately 840 to

1230 MeV/c^2. Because of the experimental placement of the neutron detectors in the forward direction, the events accepted were extremely peripheral corresponding to squared four-momentum transfers (t) that were very nearly equal to the minimum squared four-momentum transfer (t_{min}). Charged particles were detected in the Argonne Effective Mass Spectrometer[5] and/or scintillation detectors surrounding the hydrogen target.

In an earlier paper we reported a Breit-Wigner analysis of the 1.98-GeV/c data.[4] In this paper both the 1.98- and 2.41-GeV/c samples are analyzed using both the Breit-Wigner and K-matrix formulations with the previously published analysis included for completeness. In addition to doubling the data base, the 2.41-GeV/c data have a markedly different background under the S^* and thus provide a check for background-induced systematics in the pole position. Both data samples are used to look for model-induced systematics in the S^* pole value.

In Sec. II the experimental apparatus and the on-line data acquisition system are described. In Sec. III the details of the data analysis are presented. The major results of the experiment are given in Sec. IV. Section V summarizes the conclusions gained from this study.

II. APPARATUS

In this section a detailed discussion of the experimental apparatus will be presented. This will include a discussion of the secondary beam, the neutron counters, various other counters and tags, the Argonne Effective Mass Spectrometer, the neutron time-of-flight system, the trigger scheme, and the shielding used to reduce the number of background neutrons. In addition, the data collection and on-line data analysis system will be explained.

Beam

The apparatus was located in an unseparated beam[5] which for negative momenta consisted mainly of pions. Protons of 12.33-GeV/c momentum were extracted from the main accelerator ring of the Zero Gradient Synchrotron (ZGS) and brought to a focus on a 0.64 cm × 0.64 cm × 10.2-cm-long copper production target. Horizontal and vertical collimators restricted the production angles of the accepted particles to be centered at 4.25° with respect to the proton beam line. The apertures of the collimators were varied to maintain a nearly constant beam intensity.

In the first stage of the beam a pair of quadrupole magnets and a pair of bending magnets created a momentum dispersed focus at a six-element momentum hodoscope which tagged individual particle momenta to ±0.25%. The total momentum spread of the beam was typically ±1.5%.

The second stage of the beam consisted of a pair of bending magnets and four quadrupole magnets which recombined momenta at a final focus located at the center of a 38.1-cm-long liquid hydrogen target. The diameter of the approximately circular focus was 2.5 cm. The position and angles of incident beam particles for events of interest were measured to better than ±1 mrad by three spark chambers upstream of the hydrogen target.

A beam signature consisted of a coincidence between the three beam-defining counters, the momentum hodoscope, and six beam-defining anticoincidence counters. Two ethylene-gas threshold Čerenkov counters provided tagging information to label incident beam particles as pions.

Beam composition varied with momentum, but a typical $\pi^-: K^-: \bar{p}$ ratio was 127:1:0.5 for the range of momenta used in the present experiment. A small μ-e contamination present in the incident beam was insignificant to the results presented in this paper.

The total incident particle flux was kept in the range from 2.5×10^5 to 3.5×10^5 per 700-msec beam spill of the ZGS. This was done in an attempt to ensure the uniformity of accidental coincidences and other rate effects.

Neutron counters

Neutrons produced in the target and arriving in the appropriate time interval subsequent to an interacted beam particle were detected 5.30 m downstream of the hydrogen target by an array of 30 neutron counters. This time interval corresponds to neutrons whose speeds were within the interval 0.17c to 0.42c. Figure 1 shows the neutron counters (labeled N) in relation to the rest of the apparatus. The array subtended angles up to 12.5° with regard to the beam and a total laboratory

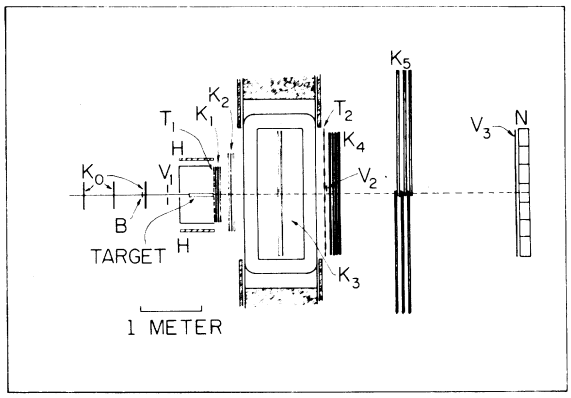

FIG. 1. Plan view of the apparatus.

solid angle of 0.098 sr. Each of the neutron counters consisted of a 30 cm × 30 cm × 15-cm-deep block of plastic scintillator, viewed from the downstream end by an Amperex 58 AVP 12.7-cm diameter photomultiplier tube. A timing signal for each counter was generated by a discriminator set at a relatively low signal level, whereas the threshold amplitude was determined by a discriminator set at a higher level. With this "high-low" system accurate timing as well as precise threshold discrimination was achieved. The counter signals were timed with respect to each other to an accuracy of ±0.2 nsec using scattered beam particles. With all counters summed together the time-of-flight spectrum for charged particles and γ rays in time with the beam showed a peak at $\beta = 1$ of 1.40 nsec full width at half maximum.

Slow neutral particles detected by the neutron counters were assumed to be neutrons, although slow neutral kaons are present at an estimated level of less than 1%. For the data presented in this paper only constrained final states are considered and therefore the neutral kaon contamination is not important. It should also be noted that γ rays from beam interactions in the target may be eliminated by virtue of their velocity. An 11-element hodoscope, labeled V_3, was located immediately upstream of the neutron counters and was used to veto charged particles which struck these counters.

The efficiency of each neutron counter is a function of photomultiplier voltage and discriminator threshold.[6] In the present experiment, the high voltages of the photomultipliers were set and maintained so that the 2.75-MeV γ ray from an Na^{24} source gave a fixed maximum pulse height. Variable attenuators were then adjusted so that the thresholds on the discriminators correspond to 3.5-MeV electron equivalent energy. For this threshold, neutron detection efficiencies ranged from 16 to 18% depending on neutron kinetic energy.[6]

Decay and trigger counters

A box of 41 scintillation counters surrounded the hydrogen target. In Fig. 1 these counters are denoted by T_1 and H. These counters detected virtually all charged particles produced in an interaction and approximately 86% of all γ rays passing through H. The hodoscope T_1 was constructed from 11 counters. The pulse-height information of the central counter of this array was used to tag those events which had two or more charged particles simultaneously passing through this counter and is denoted by the symbol C_{DPH} for "double-pulse height."

The hodoscope H was made of two subunits, one of which was constructed from 16 elements and detected wide-angle charged particles. The second, located to the outside of the first, was a 14-element hodoscope used to detect electron showers from γ-ray conversion in two radiation lengths of lead positioned between the two subunits.

The hodoscopes T_1 and H were used in forming the spark-chamber trigger and also provided a measurement of the approximate direction and multiplicity of charged particles originating in the hydrogen target. This information was used in some of the subsequent event analysis.

A 40-element hodoscope located at the spectrometer magnet exit and labeled by T_2 in Fig. 1 was used to detect charged particles exiting the spectrometer. The counters of this hodoscope were arranged in rows of 20 10-cm-wide counters above and below the magnet midplane.

Spectrometer

A plan view of the Argonne Effective Mass Spectrometer is shown in Fig. 1 along with the previously described apparatus. The basic component of the spectrometer was a large dipole magnet which had an aperture 2 m wide by 0.66 m high. The magnet had a central field of 11.4 kG, an effective length of 1 m, and an $\int \vec{B} \cdot \vec{dl}$ which was constant to about 20% over the aperture. Further details of the spectrometer are found in Ref. 5.

The five sets of wire spark chambers K_1 through K_5 measured the angles and momenta of forward-going secondary charged particles produced in the hydrogen target. The readout of the wire chambers was accomplished by 40 magnetostrictive lines with electronics which could record up to six sparks per readout for the chamber sets K_1 and K_2, and up to four sparks per readout for the chamber sets K_0, K_3, K_4, and K_5.

The K_0, K_4, and K_5 spark chambers each had planes of horizontal and vertical wires. The K_1 and K_2 chambers both had a plane of vertical wires and planes of wires at ±30° to the vertical. These nonorthogonal planes were used to resolve ambiguities in multiple-track events. The K_3 chamber had only a plane of vertical wires which were extended outside the magnet enabling the readout to be located in a low-field region. The spatial resolution of the chambers was approximately ±0.5 mm. The single-track efficiencies are estimated to be about 96% for this experiment.

Neutron time-of-flight system

To establish the neutron time of flight a standard time-to-amplitude converter (TAC) module was used. An output pulse from the beam counter

labeled B in Fig. 1 was the "start" signal input to the TAC unit and the output pulse from one and only one of the neutron counter timing discriminators was the "stop" signal. The resulting output voltage level of the TAC unit was digitized by a high-precision analog-to-digital converter (ADC). The output of the ADC was then used to calculate the absolute value of the neutron time of flight from a linear relationship in which two values, a slope and an intercept, have been determined. The intercept value was determined from special runs in which the electronic logic was set to accept γ rays in time with the beam. The resulting spectrum gave the previously mentioned narrow 1.40-nsec [full width at half maximum (FWHM)] peak corresponding to $\beta = 1$ flight times. To establish the slope a crystal controlled oscillator accurate to a few parts in 10^6 was used to input accurately known absolute time intervals into the TAC-ADC system and thereby the time interval per ADC channel was measured.

Trigger scheme

The design of the triggering scheme was dictated by the simultaneous desire to eliminate elastic scattering events and to maximize the detection of the $\pi^+\pi^- n$, $K^+K^- n$, and $\pi^+\pi^-\pi^0 n$ final states. Most of the data were taken with a trigger which could be satisfied in any one of three independent ways. This so-called "threefold" trigger consisted of one of the following requirements: (1) an incident beam particle, at least one particle in any counter of T_1 except the double-pulse-height counter (C_{DPH}) located at the center of the array (mentioned earlier), at least one particle in T_2 following the magnet, and one and only one neutron-counter (N) signal, or (2) an incident beam particle, at least one particle in C_{DPH}, at least one particle in T_2, at least one particle in the inner subsection of H, and one and only one neutron-counter signal, or (3) an incident beam particle, at least two particles in C_{DPH}, at least one particle in T_2, and one and only one neutron-counter signal. A potential event was vetoed if any particle was detected in the beam-halo counter V_1, the beam-veto counter V_2, or that element of the charged-particle-veto hodoscope V_3 covering the counter which detected the neutron. Symbolically this trigger may be summarized as

$$(1)\ 1B \cdot 1T_1\ (\text{except } C_{\mathrm{DPH}}) \cdot 1T_2 \cdot 1N,$$

or

$$(2)\ 1B \cdot 1C_{\mathrm{DPH}} \cdot 1H \cdot 1T_2 \cdot 1N,$$

or

$$(3)\ 1B \cdot 2C_{\mathrm{DPH}} \cdot 1T_2 \cdot 1N,$$

where B denotes an incident beam particle.

For a portion of the running at 2.41 GeV/c a "twofold" trigger was employed. This trigger was designed to reduce the $\pi^+\pi^- n$ one-constraint (1C) final state and thereby enhance the 4C and 3C $\pi^+\pi^- n$ final state. This trigger consisted of either one of the following two requirements: (1) an incident beam particle, at least one particle in any counter of T_1 except C_{DPH}, no particles in H, at least one particle in T_2, and one and only one neutron-counter signal, or (2) an incident beam particle, at least two particles in C_{DPH}, at least one particle in T_2, no particles in H, and one and only one neutron-counter signal. Once again a potential event was vetoed if any particle was detected in V_1, V_2, or that portion of V_3 covering the neutron counter which detected the neutron. Summarizing this trigger symbolically we have

$$(1)\ 1B \cdot 1T_1\ (\text{except } C_{\mathrm{DPH}}) \cdot \overline{H} \cdot 1T_2 \cdot 1N$$

or

$$(2)\ 1B \cdot 2C_{\mathrm{DPH}} \cdot \overline{H} \cdot 1T_2 \cdot 1N.$$

Shielding

Considerable shielding was required to reduce background neutron events. This shielding acted to absorb much of the low-energy component of background room neutrons and to thermalize higher-energy room neutrons. In addition, a Borax enclosure was built around the neutron counters themselves. Boron, a constituent of Borax, has a 759-b total thermal neutron absorption cross section. The absorption length for this process is 1.3 mm. In the present case, approximately 10 absorption lengths of Borax were used in the enclosure and consequently virtually all of the thermal neutrons surviving the concrete were eliminated.

But even with the above shielding, problems with spurious neutron triggers were still experienced. These accidental events are probably due to residual background neutrons and γ rays produced by secondary interactions of the original reaction products from the hydrogen in the decay counters, wall, etc. It should also be understood that these spurious events could only be eliminated by the use of kinematic constraints.

Data collection and on-line analysis

The spectrometer was on-line to an EMR-6050 computer whose primary function was to collect the data from up to 17 triggers per ZGS pulse and to store the results on magnetic tape during the 3.5 seconds between beam bursts. The raw data were supplied to the computer through the Science Accessories Corporation's Multiple Input Data

Acquisition System (MIDAS). The data consisted of (1) the contents of six scalars for each of 12 spark-chamber readouts, and the contents of four scalars for each of 28 readouts, (2) tag bits indicating which scintillation counters had fired for each event, including the momentum hodoscope, the beam-veto counters, the 30 counters of hodoscope H, the 11 counters of hodoscope T_1, the 40 counters of hodoscope T_2, the 11 counters of hodoscope V_3, and the 30 neutron counters, (3) tag bits indicating beam-particle identity, (4) a bit indicating the passage of an extra beam track through the apparatus in the time between the interaction and the spark-chamber firing, and (5) 12 bits of neutron time-of-flight information. For each event, 204 24-bit words were written on magnetic tape.

In the time between beam pulses, the computer also analyzed approximately 35% of the events, monitored spark-chamber efficiencies and scintillation-counter rates, and provided an oscilloscope display of reconstructed tracks from selected events and of histograms accumulated by the final-state analysis program. The powerful diagnostic tool provided by the on-line computer system[7] allowed the experiment to be tuned and debugged quickly, helped maintain a consistently high level of hardware performance during the data taking, and made feasible the on-line study of possible systematic effects.

III. DATA REDUCTION AND ANALYSIS

The data from this experiment correspond to a total flux of 45.3×10^9 pions incident on the hydrogen target: 8.2×10^9 pions with the threefold trigger at a beam momentum of 1.98 GeV/c, 22.7×10^9 pions with the threefold trigger, and 14.4×10^9 pions with the twofold trigger at 2.41 GeV/c. In this section a detailed discussion of the data analysis will be given. This will include a discussion of the off-line data analysis program, the methods used to select events of various constrained final states, the algorithm used to locate the vertex of tracks, and the geometric acceptance of the apparatus. But before this detailed description of the analysis system is given, two topics need to be presented which provide essential background, namely the kinematics of the reaction $\pi^-p\to X^0n$ and the contributions to the mass uncertainty.

Kinematics

The symbols M, E, $\vec{p}$, T, and $\beta=v/c$ with an appropriate subscript denote the mass, total energy, momentum, kinetic energy, and velocity of a particle or combinations of particles. All of these variables are taken to be in the laboratory frame of reference unless indicated otherwise. Applying energy and momentum conservation to the reaction $\pi^-p\to X^0n$ we have

$$M^2=M_{\pi^-}{}^2+M_p{}^2+M_n{}^2+2(E_{\pi^-}M_p-E_{\pi^-}E_n-M_pE_n+|\vec{p}_{\pi^-}||\vec{p}_n|\cos\theta_n)\,. \tag{1}$$

Here M is the mass of the X^0 and θ_n is the polar angle of the neutron to the beam. The variation of M with the three independent variables $|\vec{p}_{\pi^-}|$, $|\vec{p}_n|$, and θ_n is given by

$$M\frac{\partial M}{\partial|\vec{p}_{\pi^-}|}=|\vec{p}_n|\cos\theta_n-\beta_{\pi^-}(E_n-M_p)\,, \tag{2}$$

$$M\frac{\partial M}{\partial|\vec{p}_n|}=(E_{\pi^-}+M_p)(\beta_c\cos\theta_n-\beta_n)\,, \tag{3}$$

$$M\frac{\partial M}{\partial\theta_n}=-|\vec{p}_{\pi^-}||\vec{p}_n|\sin\theta_n\,. \tag{4}$$

β_c is the velocity of the center of mass.

In general a high-resolution measurement of M requires accurate knowledge of $|\vec{p}_\pi|$, $|\vec{p}_n|$, and θ_n. However, certain kinematic regions can be chosen in such a way that one or more of the differential coefficients in (2)–(4) are close to zero, thus reducing the required precision of the relevant variables.

In the present experiment the neutron counters were placed near 0° with respect to the incident beam direction. This was done for two reasons. First, we desired to duplicate as closely as possible a previous experiment which reported narrow mesons.[8] In that experiment the neutron counters were located near 0°. Second, the geometric constraints imposed by the layout of the Argonne Effective Mass Spectrometer required the neutron counters to be placed near 0°. Neutrons produced at large angles in the hydrogen target pass through the steel of the pole pieces of the spectrometer's magnet. Since the neutrons are near 0°, then by Eq. (4) $\partial M/\partial\theta_n$ will be nearly 0. Consequently a high-resolution measurement of M under these kinematic conditions requires only an accurate measurement of the magnitude of the beam and neutron momenta, with only a relatively coarse measurement of the neutron angle.

Figure 2 shows the calculated relationship between M and the neutron time of flight for a 1.98-GeV/c incident pion and a neutron flight path of 5.30 m centered on the beamline. The two values of time of flight at a given mass value correspond to the neutron going forward and backward in the center-of-mass system. In the present experiment, only events with neutron time-of-flight values in the interval 42 to 103 nsec were accepted. The 42-nsec cutoff in the time of flight at both

1.98 and 2.41 GeV/c means that only those neutrons emitted near 180° in the center-of-mass system were detected. Consequently in the case of two-body processes these neutrons correspond to the X^0 system being produced at essentially 0°.

The range of θ accepted by the neutron detectors may be converted to a range of t, the squared four-momenta transfer from the target proton to the recoil neutron:

$$t = (\tilde{p}_p - \tilde{p}_n)^2 = (M_n - M_p)^2 - 2T_n M_p, \quad (5)$$

where $\tilde{p}_p$ and $\tilde{p}_n$ are the four-momenta of the proton and neutron. Figure 3 presents a plot of t versus M for the two extreme angles of the neutron detectors at 1.98 GeV/c. The lower curve corresponds to a laboratory angle of 0.0° ($t \equiv t_{\min}$) and the upper curve to an angle of 12.5°. The essential point of this figure is that the data are taken at t values very nearly equal to $t_{\min}$, but the t values do vary as a function of M. A similar range of t is covered at a beam momentum of 2.41 GeV/c.

Mass uncertainty and mass resolution

Experimental mass uncertainty and mass resolution are both quantities which enter into the data analysis. Uncertainty in the mass scale arises because of three independent effects: (1) the absolute uncertainty in the time-interval measurement associated with the measurement of the time of flight, (2) the absolute uncertainty in the length of the flight path, and (3) the absolute uncertainty of the beam momentum. In the present experiment the systematic error in the time interval is mass dependent and is estimated in the case of the 1.98-GeV/c data to be ±0.18 nsec at the ω^0-meson mass (783 MeV/c^2) and ±0.11 nsec at the K^+K^- threshold (987 MeV). At 2.41 GeV/c the error in the time of flight was estimated to be ±0.19 nsec at 840 MeV and ±0.14 nsec at 987 MeV. At both 1.98 and 2.41 GeV/c the absolute error in the 5.30-m flight path was estimated to be ±0.25% while the error in the beam momentum was estimated to be ±1%. Table I gives for each of these errors the corresponding error in the absolute mass. Note that the dominant errors are associated with the beam momentum.

When the 1.98-GeV/c data were first analyzed from the raw-data tapes, they were processed at a nominal beam momentum of 1.96 GeV/c. At the conclusion of this analysis two facts concerning the mass scale were observed which led us to the conclusion that the beam momentum should be raised by approximately 1%. First, an ω^0-meson signal was observed which was approximately 4 MeV below the known ω^0-meson mass of 782.7 MeV/c^2. Second, the edge of the K^+K^- threshold was observed to be some 5 MeV/c^2 below its calculated value of 987.4 MeV/c^2. From Table I it may be seen that a 1% increase in beam momentum would put the threshold edge and the ω^0 mass at nearly their proper values. So we decided to reanalyze the 1.96-GeV/c data from the generated

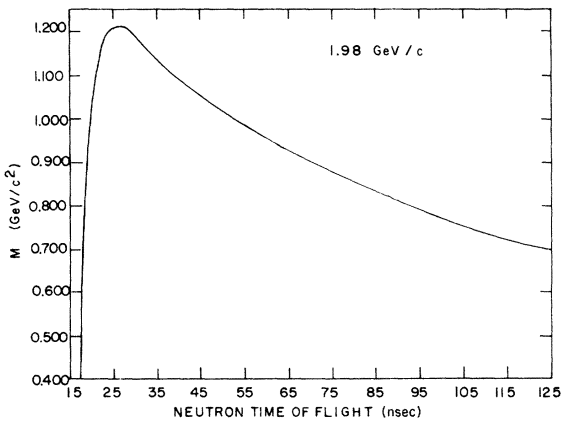

FIG. 2. Missing mass versus neutron time of flight for a 1.98-GeV/c pion beam.

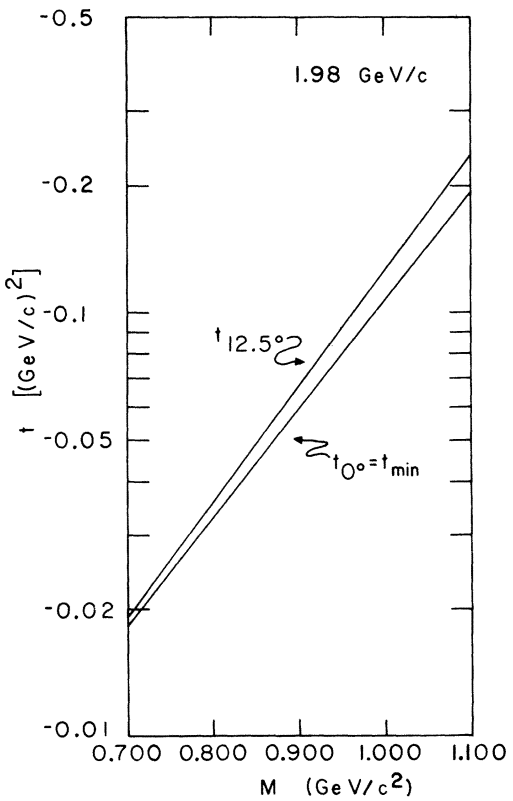

FIG. 3. Four-momentum transfer squared versus missing mass in the reaction $\pi^- p \to X^0 n$ at 1.98 GeV/c for laboratory angles corresponding to the center and outer edges of the neutron counter array.

TABLE I. Error sources contributing to absolute mass uncertainty.

Error	Source	Mass (MeV/c^2)	Beam momentum (GeV/c)	Error in missing mass (MeV/c^2)
±0.18 nsec	Time interval	783	1.98	±0.62
±0.11 nsec	Time interval	987	1.98	±0.78
±0.25%	Flight path	783	1.98	±0.84
±0.25%	Flight path	987	1.98	±0.94
±1.0%	Beam momentum	783	1.98	±3.98
±1.0%	Beam momentum	987	1.98	±5.35
±0.19 nsec	Time interval	840	2.41	±0.68
±0.14 nsec	Time interval	987	2.41	±0.80
±0.25%	Flight path	840	2.41	±0.92
±0.25%	Flight path	987	2.41	±1.03
±1.09%	Beam momentum	840	2.41	±4.24
±1.09%	Beam momentum	987	2.41	±5.13

summary tapes and raise the beam momentum 1% (within the error quoted in Table I) to 1.98 GeV/c. All of the 1.98-GeV/c mass spectra presented in this paper are from this second analysis.

The evidence at 2.41 GeV/c, while not so compelling as that at 1.98 GeV/c, suggested the need for an equivalent 1% shift. Because of cost limitations and the relatively small size of the effect, the data were not reprocessed, but the resulting mass spectra were adjusted before final analysis. These adjustments involved an upward shift in the mass scale of 3 to 5 MeV/c^2.

Our mass resolution depended on two independent effects. The first effect was the momentum uncertainty of a particular beam particle. This was due to both the physical size of a single beam momentum hososcope element and the finite extent of the beam spot. As mentioned earlier in Sec. II a particular element of our momentum hodoscope could tag an individual beam particle to ±0.25%. The other effect contributing to our mass resolution was the momentum uncertainty of a detected neutron. There were two contributions to this uncertainty. The first was the fact that it was not known at what point in the 15-cm-deep scintillator the neutron interacted. Thus the exact flight path of the neutron was uncertain. For neutrons near $\beta = 1$ (high-mass events) this contribution was of little consequence. For slower neutrons this contribution dominated. The second contribution to the momentum uncertainty of the detected neutron was the time resolution of the 30 neutron detectors. This contribution was 1.40 nsec (FWHM) as determined from the width of the previously mentioned (in Sec. II) $\beta = 1$ peak. This latter contribution becomes dominant at high values of M. The total resulting resolution of these two effects is presented in Table II for several values of M.

Off-line analysis—program EMSOF

The data were processed using an approximately modified version of the standard Effective Mass Spectrometer routine EMSOF.[9] EMSOF is an off-line program to reconstruct tracks through the wire spark chambers of the Argonne Effective Mass Spectrometer. Programming instructions were added which implemented a new vertex-finding algorithm, a new histogramming package, a new subroutine to separate constrained final states, a subroutine which handled data from some one hundred new scintillation counters, and a routine to write summary tapes. Also, many of the standard EMSOF subroutines were somewhat modified to meet the needs of the experiment.

Event selection

Events to be considered were divided into three classes before a final-state hypothesis selection. Class 1 events had two charged particles of opposite polarity momentum analyzed in the spectrometer. Class 2 events had one charged-particle momentum analyzed and a second particle had only its polar and azimuthal angles measured in the spark-chamber sets K_1 and K_2. Class 3 events had one momentum analyzed track and no further spec-

TABLE II. Total mass resolution for several different mass values.

Missing mass (M) (MeV/c^2)	Beam momentum (GeV/c)	Mass resolution (MeV/c^2) (FWHM)
800	1.98	7.4
900	1.98	9.0
1000	1.98	11.1
900	2.41	8.5
1000	2.41	10.3
1100	2.41	12.5

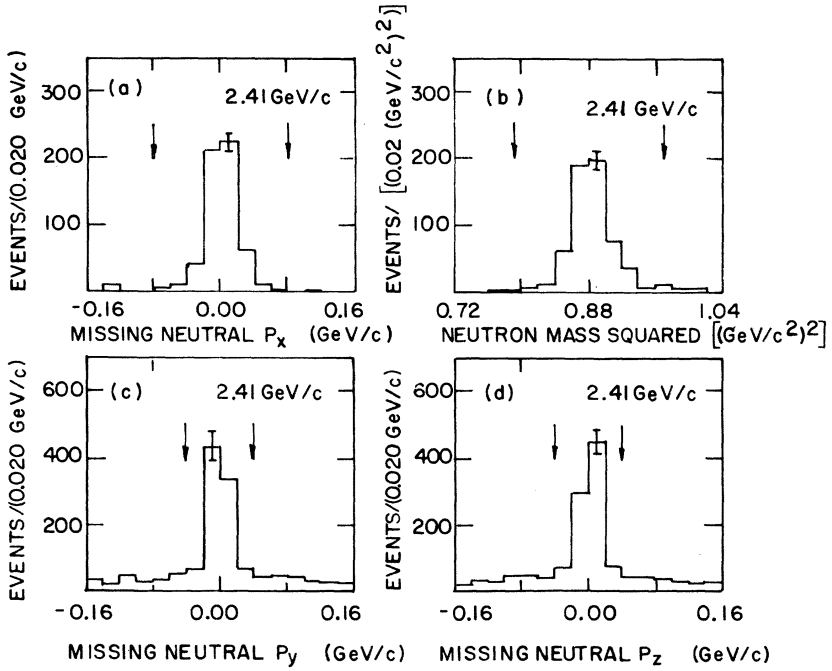

FIG. 4. The four constraints used to select the 4C $\pi^+\pi^-n$ events at 2.41 GeV/c. The cuts used to select the final data sample are indicated by arrows.

trometer information. For each event class, various final-state hypothesis assignments were attempted.

Class 1 events, those having two momentum analyzed tracks through the spectrometer, were investigated as possible candidates for the reactions

$$\pi^- p \to \pi^+ \pi^- n, \tag{6}$$

$$\pi^- p \to K^+ K^- n, \tag{7}$$

$$\pi^- p \to \pi^+ \pi^- \pi^0 n. \tag{8}$$

Class 2 and 3 events in which only one particle was momentum analyzed could only be examined as possible candidates for reactions (6) and (7).

In the case of class 1 events, reactions (6) and (7) have four constraints since all of the kinematic variables were measured in the final state. The constraints employed were 3-momentum balance plus the calculated mass squared of the neutron. Figure 4 displays histograms of these constraints for the $\pi^+\pi^-n$ final state at 2.41 GeV/c together with the cuts indicated by arrows used to select the final data sample. In our coordinate system x is the beam direction and z is upward. Similar constraints were obtained at 1.98 GeV/c.

In the case of 4C events of reactions (6) and (7) the invariant mass of the $\pi^+\pi^-$ or K^+K^- system may be calculated in two independent ways. First, one may use the beam and neutron four-vectors to establish the missing mass of the $\pi^+\pi^-$ or K^+K^- system. Second, one may use the four-vectors of the pions or kaons as measured by the spectrometer to establish the effective mass of the $\pi^+\pi^-$ or K^+K^- system. Figures 5 and 6 show the difference between these two masses for the 1.98-GeV/c $\pi^+\pi^-$ and K^+K^- data. The figures show an agreement to within 10 MeV/c^2 between the effective-

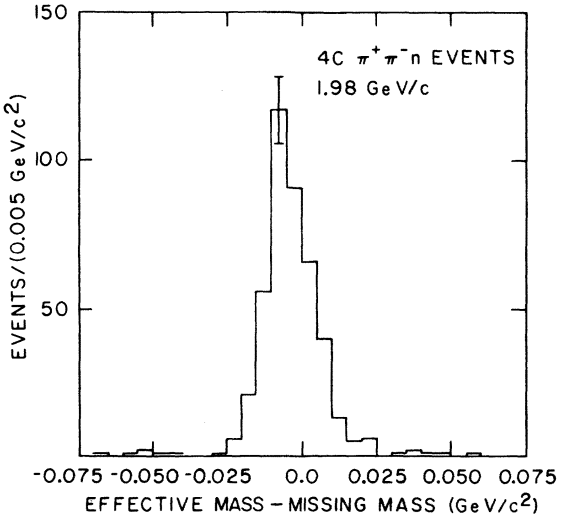

FIG. 5. The difference between the spectrometer measurement of the dipion mass and the missing mass for the reaction $\pi^- p \to \pi^+ \pi^- n$ at 1.98 GeV/c.

mass and missing-mass scales. Similar agreement was obtained at 2.41 GeV/c.

Class 1 events were then analyzed as possible candidates for reaction (8). The reaction in this case has only one constraint since the polar angle, azimuthal angle, and the magnitude of the momentum of the π^0 were not measured. The one constraint was calculated by considering the reaction to proceed as

$$\pi^- p \to \pi^+\pi^-\pi^0 B\,. \tag{9}$$

In Eq. (9) the $\pi^+\pi^-\pi^0$ is hypothesized and from energy and momentum conservation and the knowledge of the velocity of the detected baryon B, it was possible to calculate the mass of the baryon. In Fig. 7 the mass of B is plotted for the 1.98-GeV/c data. The asymmetry of the neutron signal on the high side is due to the presence of K^+K^-n events in which the detected neutron did not come from the event. The final event selection was made by requiring the mass of B to be in the range appropriate to the neutron, 0.925 to 0.980 GeV/c^2. The ω^0 meson (to be discussed later in Sec. IV) was observed in this event sample.

Class 2 events had one particle momentum analyzed and a second particle which went only through the spark chamber sets K_1-K_2. This second particle had its polar and aximuthal angles measured, but there was no measurement of the magnitude of its momentum. Consequently, three constraints were available that could be applied to select reactions (6) and (7). The three constraints used require some explanation. From the neutron information the energy (E_{X^0}) and the three-momentum ($\vec{p}_{X^0}$) of the X^0 were calculated for each event. Now if one assumes, for example, that the two particles are pions and that pion number 1 was the momentum-analyzed particle, then from energy and momentum conservation and the measured value of θ_1 it is possible to calculate both θ_2 and $|\vec{p}_1|$. The variables

$$\Delta\theta = \frac{\cos\theta_2^{\text{measured}} - \cos\theta_2^{\text{calculated}}}{\sin\theta_2^{\text{calculated}}} \tag{10}$$

and

$$\frac{\Delta P}{P} = \frac{|\vec{P}_1|^{\text{measured}} - |\vec{P}_1|^{\text{calculated}}}{|\vec{P}_1|^{\text{calculated}}} \tag{11}$$

can then be formed, allowing a comparison between predicted and measured values to be made. $\Delta\theta$ and $\Delta P/P$ as defined above form two of the three available constraints.

If X^0 is either $\pi^+\pi^-$ or K^+K^- then the angle between the planes formed by the vector P_{X^0} and the unit vectors in the direction of the two charged particles must be zero to ensure the conservation of momentum. The coplanarity angle, $\Delta\phi$, between the two planes forms the third constraint. $\Delta\theta$, $\Delta P/P$, and $\Delta\phi$ are shown in Fig. 8 for the 1.98-GeV/c data with the cuts used to select $\pi^+\pi^-n$ events indicated by arrows. At 2.41 GeV/c, a similar set of constraints was obtained.

Class 3 events had one momentum-analyzed track and no further spectrometer information. For the $\pi^+\pi^-n$ and K^+K^-n final states they are 1 constraint; the constraint used is the $\Delta P/P$ constraint described above for class 2 events. Further reduction in the background to the $\pi^+\pi^-$ and K^+K^- final states was obtained by requiring that the second meson, not seen by the spark chambers,

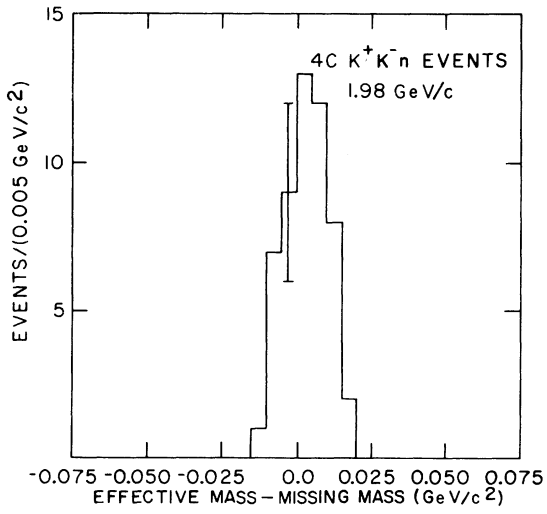

FIG. 6. The difference between the spectrometer measurement of the dikaon mass and the missing mass for the reaction $\pi^- p \to K^+K^-n$ at 1.98 GeV/c.

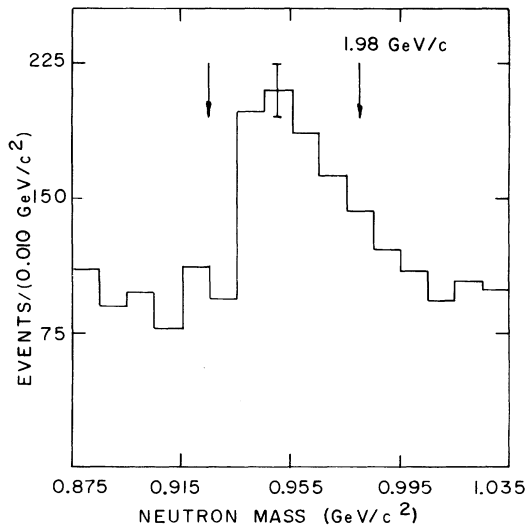

FIG. 7. The constraint used to select the $\pi^+\pi^-\pi^0 n$ final state at 1.98 GeV/c.

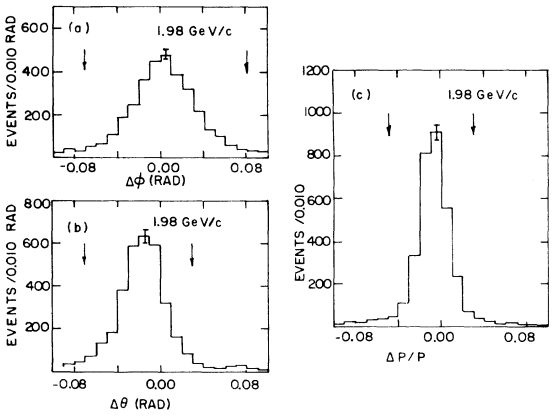

FIG. 8. The three constraints used to select the 3C $\pi^+\pi^- n$ events at 1.98 GeV/c.

be detected by the appropriate counter element of the hodoscope surrounding the hydrogen target.

In Fig. 9 $\Delta P/P$ is presented for these potential 1C $\pi^+\pi^- n$ events at 2.41 GeV/c (a) without counter selection, (b) with counter selection. Note the strong suppression of the background with little loss in the $\pi^+\pi^- n$ signal that the counter requirement imposes on the data. A similar result was obtained at 1.98 GeV/c.

Table III presents the signal-to-noise ratio of all constrained final states previously considered at both 1.98 and 2.41 GeV/c.

Target vertex

The vertex location of momentum-analyzed tracks was determined by the minimization of a χ^2 defined for the hypothesis that all the tracks originated at one point. An attempt was first made to locate the vertex of the beam and all momentum-analyzed tracks. If the χ^2 of the fit was greater than 50, the worst track was eliminated and the fit repeated.

An attempt was then made to locate the vertex of

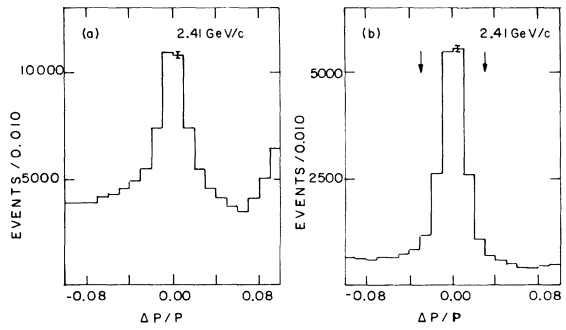

FIG. 9. The constraint used to select the 1C $\pi^+\pi^- n$ events at 2.41 GeV/c. (a) The constraint without the correct T_1 or H counter being required. (b) The constraint with the correct T_1 or H counter being required.

TABLE III. Signal-to-noise ratios for various constrained final states.

Final state	Constraint class	Beam momentum (GeV/c)	Signal-to-noise ratio
$\pi^+\pi^- n$	4C	1.98	180.
$\pi^+\pi^- n$	3C	1.98	22.3
$\pi^+\pi^- n$	1C	1.98	9.7
$K^+K^- n$	4C	1.98	7.1
$\pi^+\pi^-\pi^0 n$	1C	1.98	0.8
$\pi^+\pi^- n$	4C	2.41	58.7
$\pi^+\pi^- n$	3C	2.41	13.0
$\pi^+\pi^- n$	1C	2.41	3.1
$K^+K^- n$	4C	2.41	6.7

any other lines found in the chamber sets K_1-K_2 with the beam. The method used was the distance of closest approach. Any line whose distance of closest approach with the beam was greater than 0.4 in. was immediately rejected. A mean vertex was then calculated which was the average value of the vertex formed by any of the momentum-analyzed tracks and of the vertices formed by the K_1-K_2 lines and the beam. Any K_1-K_2 line whose distance from this mean vertex was greater than 1.0 in. was eliminated. A new mean vertex was calculated and the above procedure repeated. The mean vertex where all of the K_1-K_2 lines were within the cutoff distance of 1 in. formed the final vertex.

The distribution of vertices for the 2.41-GeV/c class 1 events and the location of the liquid hydrogen target was shown in Fig. 10. The interactions in the 0.16-cm-thick double-pulse-height counter of the T_1 array are clearly evident just beyond the downstream edge of the target. The rise in the number of events across the target in Fig. 10 is a reflection of the acceptance of the spectrometer. The acceptance for events produced at the downstream edge of the target is about a factor of 2

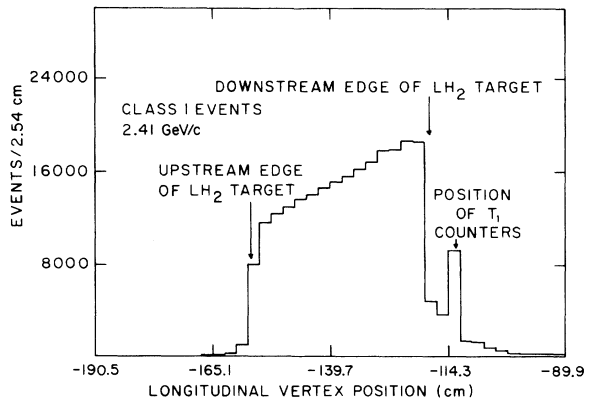

FIG. 10. The distribution of vertices and the location of the liquid hydrogen for class 1 events at 2.41 GeV/c.

higher than the acceptance for events produced at the upstream edge. All events used in the analysis were required to have a vertex within the target, thereby eliminating non-hydrogen-associated events. The vertex position in the hydrogen target also enabled the neutron flight path to be corrected for the target interaction point.

Geometric acceptance

A Monte Carlo calculation of the spectrometer acceptance was performed in the case of the $\pi^+\pi^-n$ final state for each of the three constraint classes mentioned above. At discrete values of M, events were generated which, like the data, uniformly populated the neutron counters. Decay pions from the X^0, which was assumed to be spin zero, were propagated through the spectrometer and determined to be 4C, 3C, 1C, or undetectable events depending on which spark chambers intercepted the trajectories. For purposes of field integration, a square field with vertical focusing was found to be adequate after comparison with a sample of events processed using a full inhomogeneous field integration. Corrections were made for absorption in the target and surrounding counters and for in flight decays.

The successfully detected $\pi^+\pi^-n$ events by class were then transformed into the X^0 Gottfried-Jackson (GJ) rest frame. For our highly peripheral events, the Lorentz transformation to the GJ rest frame was essentially along the beam direction. Figure 11 shows the acceptance curves generated by the Monte Carlo calculation along with the $\pi^+\pi^-n$ event histograms from the 1.98-GeV/c data. 4C events were found to populate a π^+ polar angle $\theta^{\pi^+}_{GJ}$ region near 90° in the X^0 rest frame as shown by the curve in Fig. 11(a). After transformation into the laboratory frame, the π^+ and π^- are forward going and approximately symmetric with respect to the beamline as required in order to get two trajectories passing through the spectrometer. At the other extreme, the 1C events are produced with the π^+ either parallel or antiparallel to the beam direction. This gives one particle through the spectrometer while the second misses altogether. The acceptance for the 1C events is shown in Fig. 11(c). The 3C event acceptance is intermediate between the other two classes in angle as can be seen. Of particular significance is the symmetry of the efficiency about 90° in the GJ system. The data as represented by the histogram show an asymmetry about 90° of the three classes. This asymmetry is due to the interference of a relatively small ρ signal with other non-ρ amplitudes and this effect will be further discussed in the next section. Figure 12 presents the acceptance of the Monte Carlo generated events as a function of M

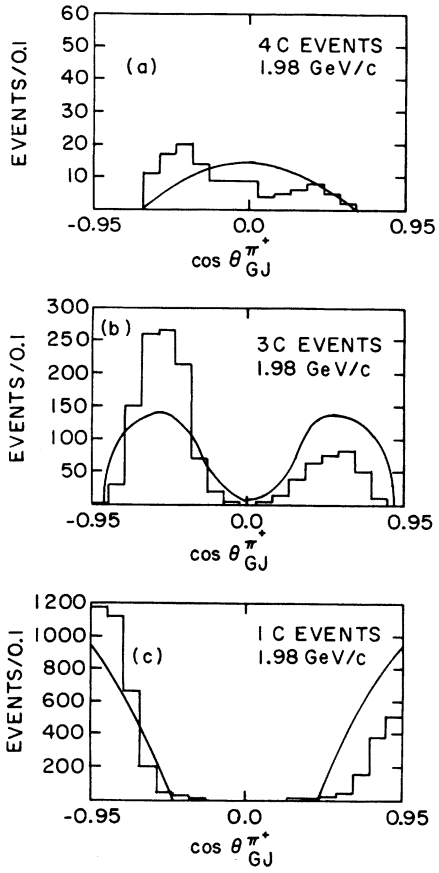

FIG. 11. The distributions in $\cos\theta^{\pi^+}_{GJ}$ for the three classes of $\pi^+\pi^-n$ events at 1.98 GeV/c for the missing-mass range $760 \le M \le 840$ MeV/c^2. The curves are from Monte Carlo generated events.

integrated over θ_{GJ} for the two beam momenta of 1.98 and 2.41 GeV/c.

Efficiencies were also generated for nonzero-X^0-spin states. The general result is that spin-projection-zero states, whose angular distributions peak near $\theta = 0°$ and 180°, tend to populate the 1C distribution, whereas nonzero projections are more important to the 3C and 4C distributions.

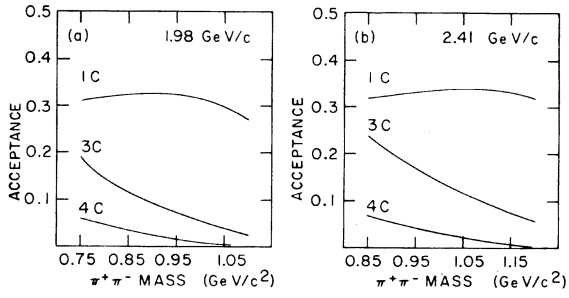

FIG. 12. The acceptance versus mass for Monte Carlo generated $\pi^+\pi^-n$ events at 1.98 and 2.41 GeV/c.

IV. RESULTS

In this section we survey the missing-mass spectra for the constrained final states at both 1.98 and 2.41 GeV/c. Results from the analysis of unconstrained final states have already been published.[10] An ω^0-meson signal observed in the mass spectrum of the 1.98-GeV/c $\pi^+\pi^-\pi^0 n$ final state is presented. In addition, a sharp break in the $\pi^+\pi^- n$ mass spectrum and a rapid rise of the K^+K^- spectrum just above threshold are observed and are associated with the S^* resonance. From fits of two models to the $\pi^+\pi^- n$ and $K^+K^- n$ spectra the position and width of the S^* pole are determined. The s-wave amplitudes from the fits are then presented in the form of Argand plots. The s-wave and p-wave amplitudes determined from the mass plots are shown to be consistent with the observed asymmetry in the $\pi^+\pi^-$ angular distribution.

Mass spectra

As discussed in Sec. III selection criteria (cuts) may be imposed on the data in an effort to isolate various final states. Table IV lists the numbers of events including background which satisfied these cuts for each final-state category.

We will first consider the mass spectra obtained from the data taken at a beam momentum of 1.98 GeV/c. These data with an analysis less extensive than that which is presented in this paper have been published previously.[4] The distribution in M for the 1C $\pi^+\pi^- n$ events is shown in Fig. 13. The full mass range of the experiment at 1.98 GeV/c extends from 770 to 1060 MeV/c^2. The data show a flat spectrum at high and low M with a rapid transition over the 40-MeV/c^2 interval between 940 and 980 MeV/c^2. We associate this dramatic drop in the cross section with the previously reported S^* resonance.[11] The normally large ρ meson signal is not apparent. Given the 11.5-to-1 signal-to-noise ratio as presented in Sec. III, we expect

TABLE IV. Number of events for various constrained final states.

Final state	Constraint class	Beam momentum (GeV/c)	Number of events in this category
$\pi^+\pi^- n$	4C	1.98	411
$\pi^+\pi^- n$	3C	1.98	3 226
$\pi^+\pi^- n$	1C	1.98	17 977
$K^+K^- n$	4C	1.98	52
$\pi^+\pi^-\pi^0 n$	1C	1.98	937
$\pi^+\pi^- n$	4C	2.41	946
$\pi^+\pi^- n$	3C	2.41	8 016
$\pi^+\pi^- n$	1C	2.41	32 688
$K^+K^- n$	4C	2.41	418

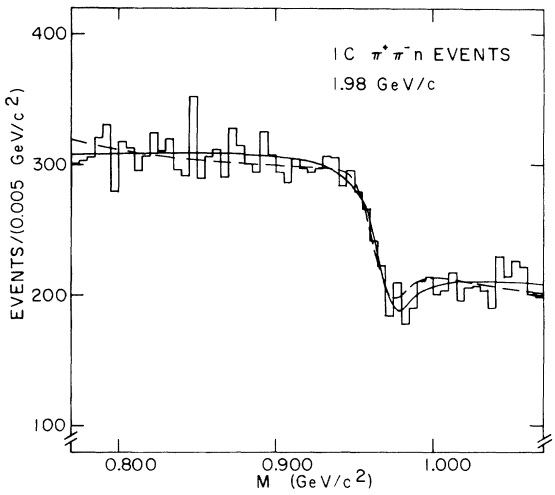

FIG. 13. Missing-mass spectrum of the 1C $\pi^+\pi^- n$ events at 1.98 GeV/c. The solid curve is a fit using the K-matrix fit corresponding to row 1 in Table V. The dashed curve is from the K-matrix simultaneous fit to both the $\pi^+\pi^-$ and K^+K^- spectra with the parameters given in the text.

an average of only 24 background events per 5 MeV/c^2 in Fig. 13.

The 3C and 4C $\pi^+\pi^- n$ M distributions are presented in Figs. 14 and 15, respectively. There are significantly fewer events in these spectra since the acceptance for these two constraint classes is much lower than for the 1C constraint class. The events are also concentrated at low mass because the acceptance for each of these constraint classes falls sharply with increasing M. However, a break is still apparent in the 3C spectrum near 950 MeV/c^2. Owing to the lower overall acceptance

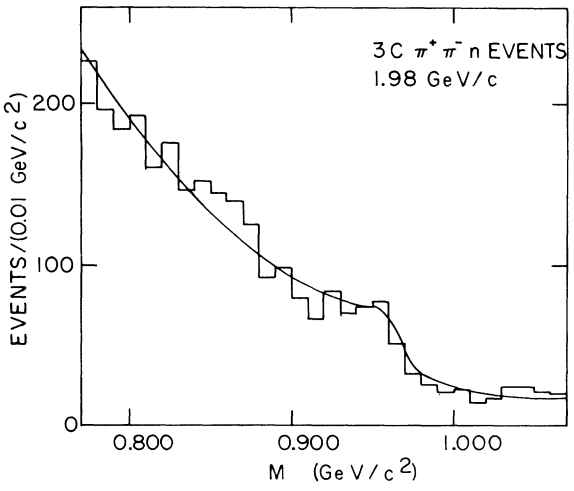

FIG. 14. Missing-mass spectrum of the 3C $\pi^+\pi^- n$ events at 1.98 GeV/c. The smooth curve is a fit using the K-matrix fit corresponding to row 2 in Table V.

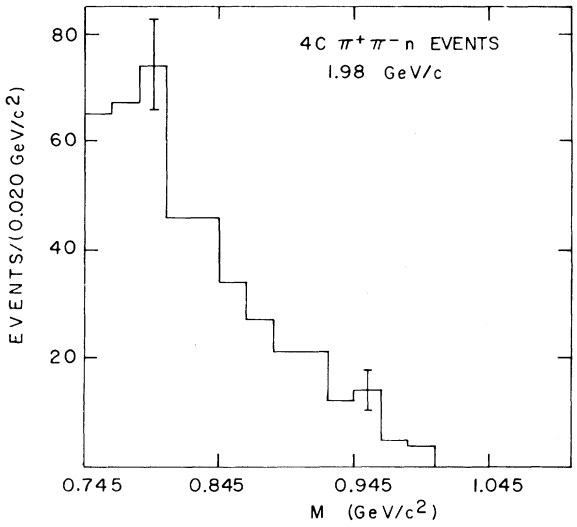

FIG. 15. Missing-mass spectrum of the 4C $\pi^+\pi^-n$ events at 1.98 GeV/c.

for the 4C class and its rapid falloff with increasing M, the 4C data are not useful in studying this effect.

The M distribution for the 1.98-GeV/c 4C K^+K^-n events is presented in Fig. 16. The previously reported[11] rapid rise of the K^+K^- mass spectrum near threshold is apparent. As was mentioned previously, we have a check on the M scale as the M spectrum for the 4C K^+K^-n events is found to be consistent within experimental resolution with a threshold at $2M_{K^+}$. The 1C and 3C K^+K^-n signals

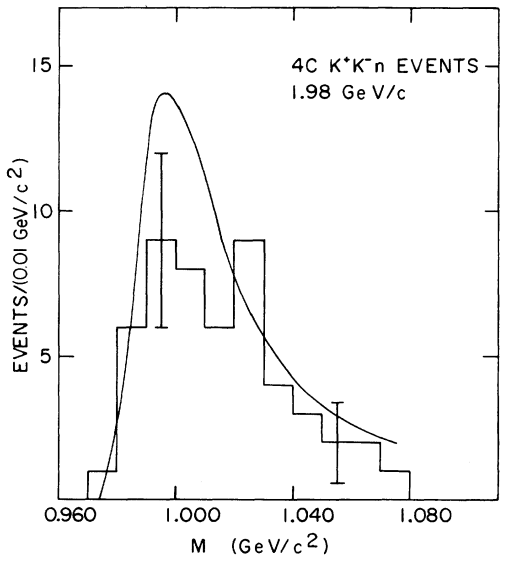

FIG. 16. Missing-mass spectrum for 4C K^+K^-n events at 1.98 GeV/c. The smooth curve is from the K-matrix simultaneous fit to both the $\pi^+\pi^-$ and K^+K^- spectra with the parameters given in the text.

are small relative to the 4C signal because near threshold both the K^+ and K^- are likely to traverse the spectrometer.

Another check on the M scale and resolution was provided by the observation of the ω^0 meson. Figure 17 shows the 1C $\pi^+\pi^-\pi^0n$ mass spectrum at 1.98 GeV/c. An ω^0 signal is evident. Even though this peak is located near our low-mass acceptance limit, an examination of our acceptance shows that it is essentially constant through the region of the figure and does not distort the ω^0 signal. The data in Fig. 17 were fitted to a Gaussian plus a constant background. The width of the ω^0 from the fit is $\Gamma = (13 \pm 3)$ MeV/c^2. After correction for our experimental resolution we find the ω^0 natural width to be (9 ± 3) MeV/c^2, which is consistent with the tabulated world average.[11] The ω^0 peak is centered at (781 ± 2) MeV/c^2, slightly below but consistent with the tabulated value of 782.6 MeV/c^2.

We now turn our attention to the mass spectra at 2.41 GeV/c. The 1C, 3C, and 4C $\pi^+\pi^-n$ M distributions at this beam momentum are presented in Figs. 18, 19, and 20. The full experimental mass range at 2.41 GeV/c extends from 845 to 1205 MeV/c^2. The 1C data of Fig. 18 show a relatively flat spectrum between 860 and 940 MeV/c^2, a rapid falloff between 940 and 980 MeV/c^2, and then a slow rise beyond 980 MeV/c^2. The 3C M distribution of Fig. 19 has a pronounced drop over the interval 940 to 980 MeV/c^2. Although less statistically significant, the 4C M spectrum presented in Fig. 20 also shows some evidence of a falloff in the (940 to 980)-MeV/c^2 region.

The M spectrum for the 2.41-GeV/c 4C K^+K^-n

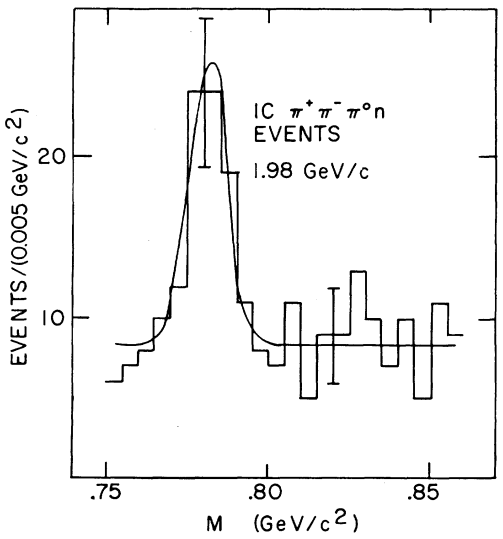

FIG. 17. ω^0-meson signal in the $\pi^+\pi^-\pi^0n$ final state from data at 1.98 GeV/c. The curve is a fit to a constant plus a Gaussian ω^0.

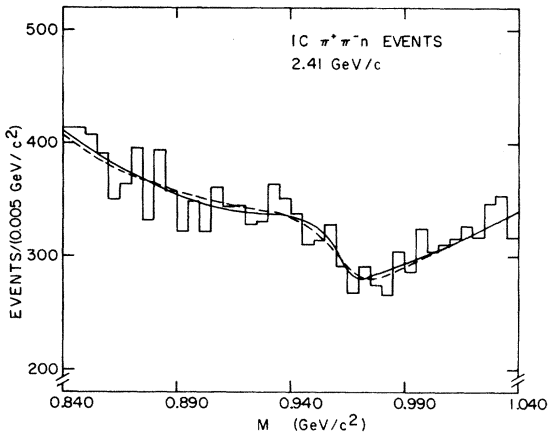

FIG. 18. Missing-mass spectrum for 1C $\pi^+\pi^- n$ events at 2.41 GeV/c. The solid curve is a fit using the K-matrix fit corresponding to row 1 in Table VI. The dashed curve is from the K-matrix simultaneous fit to both the $\pi^+\pi^-$ and K^+K^- spectra with the parameters given in the text.

events is presented in Fig. 21. Once again the rapid rise of the spectrum near the K^+K^- threshold is apparent. A small background of order 5 events/5 MeV/c^2 remains in this data sample.

The S^* resonance

In a previous paper[4] we presented an interpretation of the structure of the 1.98-GeV/c $\pi^+\pi^- n$ and $K^+K^- n$ spectra in terms of the S^* resonance. These results are repeated below for comparison. Significantly we find equivalent S^* parameters for both the 1.98- and 2.41-GeV/c data, although the data themselves appear qualitatively somewhat different.

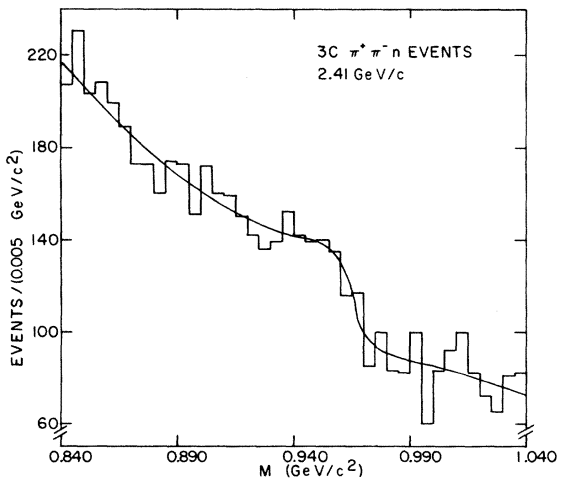

FIG. 19. Missing-mass spectrum of the 3C $\pi^+\pi^- n$ events at 2.41 GeV/c. The smooth curve is a fit using the K-matrix fit corresponding to row 2 in Table VI.

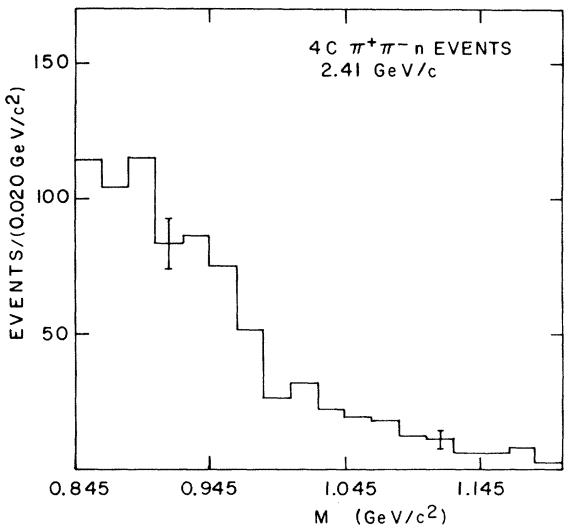

FIG. 20. Missing-mass spectrum of the 4C $\pi^+\pi^- n$ events at 2.41 GeV/c.

An alternative explanation of the observed structure in these spectra might be a cusp (threshold) phenomenon associated with the opening of the K^+K^- channel. This alone, however, is not sufficient to cause such a large effect. As Refs. 12–14 point out, any threshold effect not produced by a pole is usually too weak to be observable. Therefore an observable effect around threshold is most likely due to the presence of a pole in the complex mass plane. In the S^* parametrization the pole is explicitly given a Breit-Wigner form. If one uses a threshold parametrization in terms of the K-matrix, as discussed below, the formal-

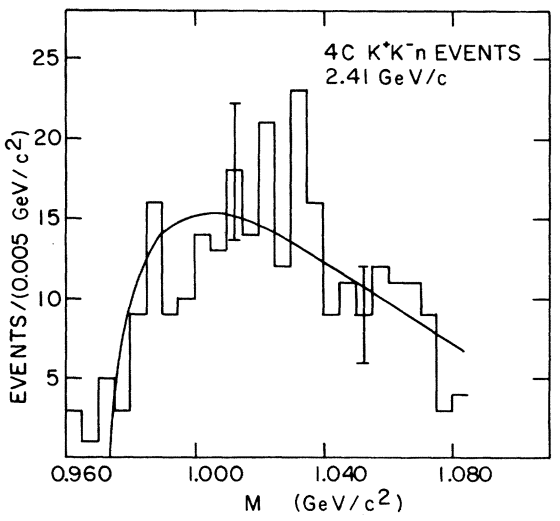

FIG. 21. Missing-mass spectrum for 4C $K^+K^- n$ events at 2.41 GeV/c. The smooth curve is from the K-matrix simultaneous fit to both the $\pi^+\pi^-$ and K^+K^- spectra with the parameters given in the text.

ism does not automatically produce a pole. The parameters which are necessary to describe the data may or may not imply a pole. As we shall see, this approach does lead to a pole at the same complex mass as found in the S^* analysis.

In most data samples a problem encountered in extracting the S^* parameters comes from the need to extract the s-wave $\pi\pi$ amplitude in the presence of larger p-wave amplitude. To do this a partial-wave analysis of the $\pi^+\pi^-$ system is employed. In our data, as is particularly evident in Fig. 13, there is no discernible ρ and hence no obvious gain to be made from such a procedure. We will return to this point later when we discuss the asymmetry ratio.

At this point a short outline of the analysis to follow is helpful. We first present a discussion of the equations appropriate for describing the $\pi\pi$ mass spectrum for both the S^* and K-matrix parametrizations. This discussion is concluded with an enumeration of parameters used in the various fits. We next present the results for fits to the $\pi\pi$ spectrum at 1.98 and 2.41 GeV/c using the two different models. A short discussion of the role of the KK spectrum in the two models is presented next. The amplitude analysis is concluded with a discussion of the simultaneous analysis of the $\pi\pi$ and KK spectra using the K-matrix parametrization.

The analysis procedure used in this paper is the minimization of the χ^2 for the hypothesis that the $\pi^+\pi^-n$ mass spectra in Figs. 13, 14, 18, and 19 are of the form

$$\frac{dN_c(M)}{dM} = J(M)F(t,M)[\epsilon_c^0(M)\,|T_\pi^0(M)|^2 + \epsilon_c^1(M)\,|T_\pi^1(M)|^2] + B_c(M)\,. \tag{12}$$

$N_c(M)$ is the number of events of constraint class c as a function of missing mass M. $J(M)$ is the solid angle subtended by the neutron counters in the overall center-of-mass frame multiplied by a normalization factor. ϵ_c^0 is the s-wave Monte Carlo efficiency for constraint class c; T_π^0 is the s-wave $\pi\pi$ scattering amplitude. ϵ_c^1 and T_π^1 are the corresponding p-wave functions. $B_c(M)$ is a background term which will be discussed in more detail in connection with the p-wave amplitude, T_π^1. We have tried fits including corresponding d-wave quantities in the form of the f meson and have found the contribution to be consistent with zero in the 1.98-GeV/c^2 data. For the fits to the 2.41-GeV/c^2 data the d-wave contribution was neglected from the outset and the fitted mass range reduced to 840 to 1070 MeV/c^2. Note that Eq. (12) implicitly assumed that an integration over angles (in the $\pi\pi$ rest frame) has been performed. The cross terms between s and p waves vanish in this integration because the calculated efficiencies are symmetric about 90°.

In a $\pi\pi$ scattering analysis of reactions 6 and 7, $F(t, M)$ would contain the virtual-pion propagator and describe the nucleon vertex. Several forms of F were examined including the one-pion-exchange (OPE) form,[15] an exponential factor $\exp(7t_{\min})$, and the product $F(t, M)J(M)$ equal to a constant. For the $\pi^+\pi^-n$ data presented, we emphasize that both the s-wave cross section and the overall quality of our fits (χ^2 probability) did not depend on the choice among these three options. Therefore, this parametrization should not be taken as implying the dominance of a particular production mechanism. Results presented in this paper have been obtained using the OPE form.

Two different parametrizations of the s-wave amplitude were used in the fitting, namely the S^* Breit-Wigner and the K-matrix parametrization of the previously mentioned threshold phenomenon. The S^* Breit-Wigner amplitude is given in the unitary form[16]

$$T_\pi^0(M) = \frac{2}{3}\left[\frac{e^{2i\delta}-1}{2i} + \frac{e^{2i\delta}\Gamma_\pi M_0}{M_0^2 - M^2 - iM_0(\Gamma_\pi + \Gamma_K)}\right], \tag{13}$$

$$\Gamma_\pi = g_\pi(\tfrac{1}{4}M^2 - M_{\pi^+}{}^2)^{1/2}, \tag{14}$$

$$\Gamma_K = g_K[(\tfrac{1}{4}M^2 - M_{K^+}{}^2)^{1/2} + (\tfrac{1}{4}M^2 - M_{K^0}{}^2)^{1/2}], \tag{15}$$

where δ, M_0, g_π, and g_K are the adjustable parameters; M_{π^+}, M_{K^+}, and M_{K^0} are the masses of the π^+, K^+, and K^0. Γ_K is the sum of the partial widths for decay to the final states K^+K^- and $K^0\bar{K}^0$. Below $K\bar{K}$ thresholds the positive imaginary square root is implied. Here the $T_\pi^0(M)$ amplitude is the sum of a background amplitude plus a Breit-Wigner amplitude. The drop occurs in the $\pi^+\pi^-n$ spectra because the phase change across the relatively narrow S^* is superimposed on a constant background phase δ. According to this view, it is then the interference between the background amplitude and the S^* Breit-Wigner amplitude that causes the sharp edge in the data. In addition, the 2π amplitude does not fully recover above the S^* because of strong absorption by the KK channel. The position of the S^* pole is by definition the complex zero of the denominator of the second term of $T_\pi^0(M)$.

The K-matrix amplitude[12,17,18] is given by

$$T_\pi^0(M) = \frac{\alpha + i\beta^2 q/(1-i\gamma q)}{1 - ik[\alpha + i\beta^2 q/(1-i\gamma q)]}, \tag{16}$$

$$k = (\tfrac{1}{4}M^2 - M_{\pi^+}{}^2)^{1/2}, \tag{17}$$

$$q = (\tfrac{1}{4}M^2 - M_{K^+}{}^2)^{1/2}, \tag{18}$$

where the K matrix is

$$K = \begin{pmatrix} \alpha & \beta \\ \beta & \gamma \end{pmatrix}, \tag{19}$$

and α, β, and γ are the adjustable real parameters. In this parameterization the position of the S^* pole is by definition the complex zero of the denominator of $T_\pi^0(M)$ in Eq. (16).

For the p-wave contribution either we use a ρ Breit-Wigner form multiplied by a Monte Carlo generated efficiency as indicated in Eq. (12) or we include the p-wave effects in the background term $B_c(M)$. The former case will be referred to as the physical background, the latter as the polynomial background. In the physical background the ρ amplitude, T_π^1, is given by

$$T_\pi^1 = \frac{r_\rho M_\rho \Gamma_\rho Y_1^0(\Omega)}{M_\rho^2 - M^2 - iM\Gamma_\rho}, \tag{20}$$

where M_ρ is the ρ mass, Γ_ρ is the ρ width, $Y_1^0(\Omega)$ is the $l=1$, $m=0$ spherical harmonic, and r_ρ is a scale factor. In fits using this background there are two parameters, r_ρ and $B_c(M)$ which is assumed to be mass independent. In the polynomial background, $B_c(M)$ is taken as a linear (two parameters) or quadratic (three parameters) function of M depending on the particular fit. The parameterization of the ρ-wave contribution is the same for both the S^* and the K-matrix analyses.

The final form of Eq. (12) in the S^* Breit-Wigner case contains either seven or eight adjustable parameters: the overall normalization, four s-wave parameters, and either two or three parameters to describe the p-wave contribution plus background. In the case of the K-matrix fits Eq. (12) has either six or seven adjustable parameters: the overall normalization, α, β, γ, and two or three parameters for the p-wave plus background contribution.

We have already noted the independence of the pole position on the form of $F(t, M)$. To check its dependence on the parameterization and background we list in Table V the pole position from various fits made to the 1.98-GeV/c 1C and 3C $\pi\pi n$ data in Figs. 13 and 14. Rows 1 and 2 list fits made using the K-matrix parameterizations in conjunction with linear and quadratic backgrounds. For reference purposes the fits to the 1.98-GeV/c $\pi\pi n$ spectra of Ref. 4 which used the S^* Breit-Wigner parametrization are included in rows 4 and 5. In row 6, a fit which used the S^* Breit-Wigner parameterization and a physical background is presented. The χ^2 probabilities for the various fits are given in column 4 of Table V. The 1C fits are excellent and the 3C fits are acceptable. The fits from rows 1 and 2 of Table V are shown as the solid curves in Figs. 13 and 14, respectively. These curves are nearly indistinguishable from the curves for the S^* parameterization shown in Ref. 4.

The results of fits to the 1C and 3C $\pi^+\pi^- n$ events at 2.41 GeV/c are presented in Table VI. Rows 1 and 2 present the K-matrix fits while rows four and five present the S^* Breit-Wigner fits. The χ^2 probabilities for the fits are once again given in column 4. All fits are seen to be acceptable. The fits from rows 1 and 2 are shown as the solid curves in Figs. 18 and 19, respectively.

There is an obvious consistency between fits to the data at 1.98 and 2.41 GeV/c and an independence from the background parameterization. The computed pole position is found to be independent of the form of the background within the computed uncertainties. The pole parameters also appear independent of the rest frame decay angles since the data from the two constraint classes sample different angular ranges. The implication of the analysis thus far is that there is a pole in the s-wave $\pi\pi$ amplitude just below the KK threshold. The pole position is well defined in the sense that it is model independent.

In the S^* analysis the position of the pole was found to be independent of the choice of the parameter g_K. In order to determine g_K it was necessary to use the K^+K^-n data. On the other hand, in the K-matrix formalism α, β, and γ may all be determined by fitting the $\pi^+\pi^-$ mass spectrum alone. Since the K^+K^- mass spectra can be fitted simultaneously with no extra parameters, this would

TABLE V. S^* pole parameters at 1.98 GeV.

Constraint class	Fit	Mass range (MeV/c^2)	Background form	χ^2 probability (%)	Pole position (MeV/c^2)
1C $\pi^+\pi^-n$	K matrix	770–1070	Linear	95	$(978 \pm 5) - i(21 \pm 5)$
3C $\pi^+\pi^-n$	K matrix	770–1070	Quadratic	11	$(965 \pm 5) - i(10 \pm 5)$
1C $\pi^+\pi^-n$ + 4C K^+K^-n	K matrix simultaneous	770–1070 / 975–1085	Linear / None	92	$(969 \pm 3) - i(14 \pm 4)$
1C $\pi^+\pi^-n$	S^* Breit-Wigner	770–1070	Linear	94	$(965 \pm 5) - i(21 \pm 5)$
3C $\pi^+\pi^-n$	S^* Breit-Wigner	770–1070	Quadratic	9	$(970 \pm 6) - i(13 \pm 5)$
1C $\pi^+\pi^-n$	S^* Breit-Wigner	770–1070	ρ Meson	82	$(967 \pm 7) - i(32 \pm 6)$

TABLE VI. S^* pole parameters at 2.41 GeV/c.

Constraint class	Fit	Mass range (MeV/c^2)	Background form	χ^2 probability (%)	Pole position (MeV/c^2)
1C $\pi^+\pi^-n$	K matrix	840–1070	Quadratic	33	$(968\pm9)-i(16\pm8)$
3C $\pi^+\pi^-n$	K matrix	840–1070	Quadratic	52	$(970\pm7)-i(12\pm6)$
1C $\pi^+\pi^-n$ + 4C K^+K^-n	K matrix simultaneous	840–1070 975–1085	Quadratic Constant = 5 events/(0.005 GeV/c^2)	22	$(976\pm8)-i(22\pm11)$
1C $\pi^+\pi^-n$	S^* Breit-Wigner	840–1070	Quadratic	34	$(970\pm8)-i(14\pm7)$
3C $\pi^+\pi^-n$	S^* Breit-Wigner	840–1070	Quadratic	53	$(968\pm7)-i(12\pm6)$

appear to be a strong point in favor of this latter model.

We complete our analysis of the mass spectra by simultaneously fitting the sample of 1C $\pi^+\pi^-n$ and 4C K^+K^-n events at 1.98 and 2.41 GeV/c using the K-matrix parametrization. To fit the K^+K^-n events the fitting function[12,17,18] used was

$$\frac{dN_K}{dM} = F(t,M)J(M)\epsilon_K^0(M)\left|T_K^0\right|^2, \tag{21}$$

$$T_K^0 = \frac{\beta/(1-i\gamma q)}{1-ik[\alpha+i\beta^2 q/(1-i\gamma q)]}. \tag{22}$$

Equations (21) and (22) are the analog of Eqs. (12) and (13) with the p-wave omitted and the s-wave amplitude replaced by the inelastic amplitude T_K^0 for the process $\pi^+\pi^- \to K^+K^-$. The efficiency $\epsilon_K^0(M)$ is the Monte Carlo generated K^+K^- acceptance.

The procedure used in fitting the data was the simultaneous minimization of a two part χ^2 using the function given in Eq. (12) with the amplitude of Eq. (16) to fit the $\pi^+\pi^-n$ portion of the data and the function given in Eq. (21) with the amplitude of Eq. (22) to fit the K^+K^-n portion of the data. Because of nonzero mass resolution, there are some K^+K^-n events below threshold. To fit these data it is necessary to include our $\sigma = 4$ MeV/c^2 resolution in the fit. Likewise even a small mass shift can affect the fits enormously. We have already observed that the mass of our ω^0 signal is 1.0 ± 2.0 MeV/c^2 low. An appropriate upward shift of the mass scale near the K^+K^-n threshold is made in compensation. We obtain a 92.2% confidence level fit shown in Fig. 13 for the $\pi\pi$ spectrum for $\alpha = 1.3\pm0.4$, $\beta = -2.9\pm0.3$, and $\gamma = -7.1\pm0.5$ These results compare favorably with $\alpha = 0.9\pm0.3$, $\beta = -3.5\pm0.4$, and $\gamma = -5.9\pm0.6$ determined by fits to the $\pi^+\pi^-n$ spectra alone. The curve for the KK spectrum generated from this fit is shown in Fig. 16. The position of the S^* pole corresponding to these values of α, β, and γ is given in row three of Table V.

A fit to the 2.41-GeV/c 1C $\pi^+\pi^-n$ and 4C K^+K^-n data was carried out using this same procedure except that a 5-event per 5-MeV/c^2 constant background was added to Eq. (21) to describe the previously mentioned background that is present in this data sample. For these data we obtain a 21.7% confidence level fit shown as a dashed curve in Fig. 18 and a solid curve in Fig. 21 for $\alpha = 1.0 \pm 0.7$, $\beta = -3.4\pm0.8$, $\gamma = -5.8\pm0.9$. The position of the S^* pole determined from these parameters is given in row three of Table VI.

Argand plots

Figure 22(a) presents an Argand plot calculated from the S^* parametrization [Eq. (13)] using the parameters given in row four of Table V. Figure 22(b) presents the equivalent plot calculated using the K-matrix amplitude with the parameters given in row one of Table V. These two plots agree reasonably well and with the results of published phase-shift analyses. Note, however, that the phase shift for masses near the real part of the pole is quantitatively quite different between the two fits. It should also be noted that the sharp left turn in the Fig. 22(b) is built into the K-matrix formalism and its derivatives (e.g., the M matrix).

Our Argand plots behave differently from those of Refs. 2 and 15 near the pole. It is interesting to note, however, that these simple s-wave fits are in good agreement with the more complex phase-shift results for masses away from the pole position.

Asymmetry ratio

No moment analysis was performed on the $\pi^+\pi^-n$ data. To carry out a moment analysis the experimental efficiency as a function of the azimuthal decay angle θ_{GJ} must be relatively uniform. This requirement is clearly not met in our data as shown in Fig. 11. It was found that the normalization problems associated with the large differences in the relative acceptances of the three-event classes and the limited statistical quality of the 3C and 4C $\pi^+\pi^-n$ events precluded an accurate determination of the full angular distribution in the

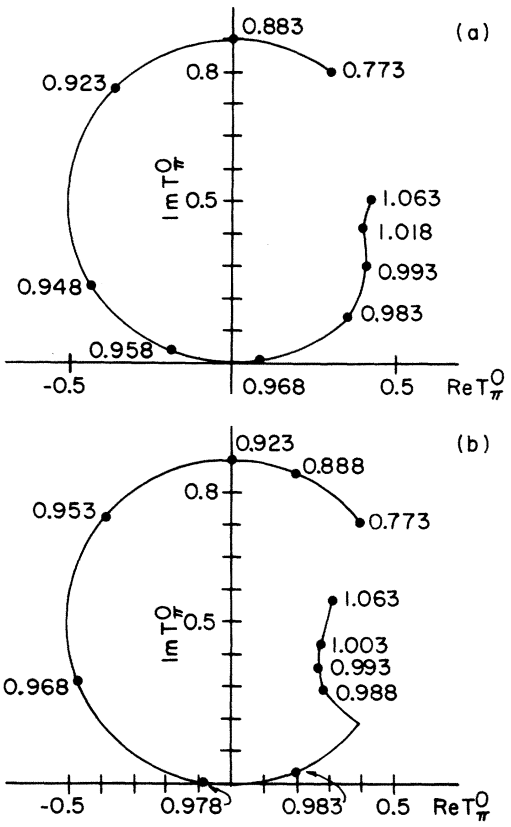

FIG. 22. Argand plots calculated from fits to the 1C $\pi^+\pi^-$ mass spectrum at 1.98 GeV/c. (a) S^* Breit-Wigner fit of row 4 in Table V. (b) K-matrix fit of row 1 in Table V.

Gottfried-Jackson frame. But even so, it is still possible to understand the asymmetry of the angular distribution shown in Fig. 11.

To understand the asymmetry present in the angular distribution a consistency argument can be made. Consider the fit to the 1C $\pi^+\pi^- n$ events listed in the last row of Table V. In this fit a background in the form of the ρ meson [Eq. (20)] is used in the parametrization of the fitting function. The resulting ρ amplitude, T_π^1, may be used in conjunction with the s-wave amplitude, T_π^0, to calculate from Eq. (12) the absolute value squared of the total amplitude

$$|T|^2 = \frac{1}{4\pi}\left[\tfrac{4}{9}|T_\pi^0|^2 + 4\,\mathrm{Re}(T_\pi^0 T_\pi^{1*})\cos\theta + 9|T_\pi^1|^2\cos^2\theta\right], \tag{23}$$

where we have included only a $\cos\theta$ dependence for the ρ p-wave amplitude. The portion of the forward and backward hemispheres where there is a large acceptance for 1C $\pi^+\pi^- n$ events is in the $\cos\theta$ interval 0.65 to 0.95 in the case of the forward hemisphere and $\cos\theta$ values in the interval -0.95 to -0.65 for the case of the backward hemisphere. After integrating over these portions of the forward and backward hemispheres to form the quantities F and B defined by

$$F = \int_{0.65}^{0.95} |T|^2 d(\cos\theta), \tag{24}$$

$$B = \int_{-0.95}^{-0.65} |T|^2 d(\cos\theta), \tag{25}$$

we can calculate an asymmetry ratio given by

$$R = \frac{F - B}{F + B}. \tag{26}$$

We find from Eqs. (24) and (25) that R is given by

$$R = \frac{4\,\mathrm{Re}(T_\pi^0 T_\pi^{1*})(0.48)}{\frac{4}{5}|T_\pi^0|^2(0.6) + 9|T_\pi^1|^2(0.39)}. \tag{27}$$

When the quantities T_π^0 and T_π^1 from the fit are evaluated at a missing mass of 800 MeV/c^2 the value of R that results is 0.64 ± 0.09. This value may be compared with one calculated from the data of Fig. 11(c) which includes the missing-mass range $760 \leq M \leq 940$ MeV/c^2. To calculate R from the data it is only necessary to do a background subtraction. In principle one should also correct the experimental distribution using the Monte Carlo acceptance. However, since this acceptance is symmetric about 90° its effect cancels out in the calculation of R. The value of R obtained from the data is 0.56 ± 0.02 in good agreement with the predicted asymmetry ratio. This experimental value was obtained directly from the data in Fig. 11(c) after doing a background subtraction corresponding to the constant background determined by the fit to the mass distribution. It was necessary to assume that this constant background was symmetric about $\cos\theta = 0$.

In summary, fits to the $\pi\pi$ mass spectrum give a small p-wave amplitude consistent with the lack of a demonstrable ρ signal in the mass spectrum. The small p-wave amplitude predicts a relatively large forward-backward asymmetry in the angular distribution which agrees with what is observed.

V. SUMMARY AND CONCLUSIONS

By studying dimeson production at very low four-momentum transfer we have obtained $\pi^+\pi^- n$ data samples with very little ρ production. As a result we have been able to study the s-wave system without first going through a partial-wave analysis to subtract out the normally present large p-wave contribution. We find that both the $\pi^+\pi^-$ and K^+K^- spectra can only be understood in terms of a narrow s-wave pole below the K^+K^- threshold which interferes with a slowly varying s-wave

background. By studying the effect in independent 1C and 3C data samples at 1.98 and 2.41 GeV/c and by using two different parametrizations (S^* Breit-Wigner and K matrix) we have tried to get a feel for statistical and systematic uncertainties in the determination of the pole parameters.

Our best value of the S^* pole is $(969 \pm 5) - i(15 \pm 4)$ MeV/c^2. This was determined by considering rows 1, 2, 4, and 5 from Tables V and VI. The K-matrix simultaneous fits to $\pi^+\pi^- n$ and $K^+K^- n$ were excluded because of the sensitivity of those fits to the absolute mass scale as pointed out in Sec. IV. The real and imaginary parts of the pole position are just the weighted average of the values given in the tables. The error in the real part is the standard deviation in the individual values added in quadrature with a 3-MeV/c^2 mass-scale uncertainty. The error in the imaginary part is just the standard deviation in the individual values.

The pole parameters as determined in this experiment differ quite significantly from the present world average of $(993.2 \pm 4.4) - i(20 \pm 3.7)$.[11] We find it highly unlikely that this discrepancy can be attributed to systematic effects in this experiment. In particular, the S^* mass is determined primarily by the place at which the sharp break occurs in the $\pi^+\pi^-$ mass spectrum and is therefore largely independent of slowly varying instrumental biases such as the acceptance as a function of $\pi^+\pi^-$ mass. We find it more likely that the difference is due to the very different nature of this experiment. With a high-statistics, high-resolution sample of dimeson events near t_{min} we have been able to study the s-wave system with a very straightforward analysis.

ACKNOWLEDGMENTS

We wish to thank the staff of the ZGS for their support. Special thanks are due to Dr. R. Diebold, Dr. D. Ayres, Dr. S. Kramer, Dr. B. Wicklund, Dr. I. Ambats, and the remaining members of the Effective Mass Spectrometer group. We acknowledge the contributions of P. Hornung, M. Anderson, and R. Boz at various stages in the experiment.

†Research supported by the U. S. Energy Research and Development Administration under Contract No. W-7405-eng-82.

*Present address: Fermi National Accelerator Laboratory, P. O. Box 500, Batavia, Illinois 60510.

[1]T. F. Hoang, Nuovo Cimento 61A, 325 (1969); T. F. Hoang *et al.*, Phys. Rev. 184, 1363 (1969).

[2]See for example S. D. Protopopescu *et al.*, Phys. Rev. D 7, 1279 (1973); B. Hyams *et al.*, Nucl. Phys. B64, 134 (1973).

[3]D. M. Binnie *et al.*, Phys. Rev. Lett. 31, 1534 (1973).

[4]M. Buttram *et al.*, Phys. Rev. D 13, 1153 (1976).

[5]For more details on the experimental apparatus see D. S. Ayres, in *Proceedings of the International Conference on Instrumentation for High Energy Physics, Frascati, Italy, 1973*, edited by S. Stipcich (Laboratori Nazionali del Comitato Nazionale per l'Energia Nucleare, Frascati, Italy, 1973), p. 665; R. Diebold, in *π-π Scattering—1973*, proceedings of the International Conference on π-π Scattering and Associated Topics, Tallahassee, 1973, edited by P. K. Williams and V. Hagopian (AIP, New York, 1973), p. 284; I. Ambats *et al.*, Phys. Rev. D 9, 1179 (1974).

[6]R. M. Jacobel, Ph.D. thesis, Iowa State University, 1973 (unpublished).

[7]C. E. W. Ward, Report No. ANL/HEP 7206, 1972 (unpublished).

[8]D. L. Cheshire *et al.*, Phys. Rev. Lett. 28, 520 (1972); R. W. Jacobel *et al.*, *ibid.* 29, 671 (1972); A. F. Garfinkel *et al.*, *ibid.* 29, 1477 (1972).

[9]R. Rivetna, Report No. ANL/HEP 7363, 1973 (unpublished).

[10]M. Buttram *et al.*, Phys. Rev. Lett. 35, 970 (1975).

[11]A complete set of references may be found in Particle Data Group, Rev. Mod. Phys. 48, S1 (1976).

[12]A. Barbaro-Galtieri, in *Advances in Particle Physics*, edited by R. L. Cool and R. E. Marshak (Interscience, New York, 1968), Vol. II, p. 220.

[13]G. F. Chew, Report No. UCRL-16983, 1966 (unpublished).

[14]W. R. Frazer and A. W. Hendry, Phys. Rev. 134, B1307 (1964).

[15]See for example P. Estabrooks *et al.*, in *π-π Scattering—1973* (Ref. 5), p. 37.

[16]S. M. Flatté *et al.*, Phys. Lett. 38B, 232 (1972).

[17]R. Levi Setti and T. Lasinski, *Strongly Interacting Particles* (Univ. of Chicago Press, Chicago, Illinois, 1973).

[18]R. H. Dalitz, *Strange Particles and Strong Interactions* (Oxford Univ. Press, New York, 1962).

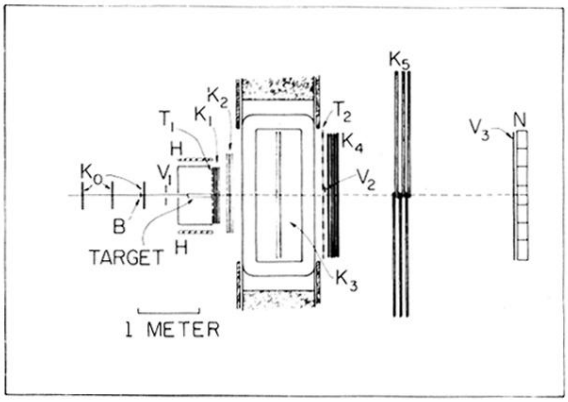

FIG. 1. Plan view of the apparatus.